

## Dynamics of the Brazil-Malvinas Confluence based on inverted echo sounders and altimetry

Gustavo Goni and Scott Kamholz

Division of Meteorology and Physical Oceanography, Rosenstiel School of Marine and Atmospheric Science  
University of Miami, Miami, Florida

Silvia Garzoli

Lamont-Doherty Earth Observatory of Columbia University, Palisades, New York

Donald Olson

Division of Meteorology and Physical Oceanography, Rosenstiel School of Marine and Atmospheric Science  
University of Miami, Miami, Florida

**Abstract.** We use data from Geosat altimeter and from 10 inverted echo sounder (IES) moorings deployed in the SW Atlantic Ocean off the Argentine continental shelf to investigate several aspects of the dynamics of the upper layer in the Brazil-Malvinas Confluence region. We use the altimeter data to estimate the sea height anomalies at each IES location and use the IES data to compute the upper layer thickness, taken in this work to go to the depth of the 8°C isotherm. We first discuss the sea height and upper layer thickness variations caused by the passage of the Brazil Current, Malvinas Current, and warm anticyclonic and cold cyclonic eddies. We introduce a two-layer model in which we decompose the sea height into its baroclinic and barotropic contributions. We then propose a method to monitor the thickness of the upper layer and the barotropic and baroclinic transports as a function of the sea height anomalies and the statistics of the upper layer thickness and reduced gravity for the region. We compute the reduced gravity values from the slope of a linear fit between the sea height anomalies and the upper layer thicknesses. We estimate the reduced gravity values for this region to range from 0.005 to 0.011 m s<sup>-2</sup>. We also estimate the mean barotropic sea height difference using two methods: conservation of mass and conservation of potential vorticity. Finally, we compute the time series for the baroclinic and barotropic transports during the Geosat Exact Repeat Mission time period. Our results suggest that the mean baroclinic transport in the upper layer decreases from 12 Sv at around 35°S to 7 Sv at 37°S. Our results also indicate that there is a significant barotropic contribution to the upper layer transport in the confluence region.

### 1. Introduction

The merger of subtropical western boundary current regimes with currents from the subpolar domains results in large contrasts in stratification. These changes in stratification and the action of eddy activity in the western boundary domain to drive barotropic flows render transport estimates in these regimes problematic. In this work we consider the decomposition of the baroclinic and barotropic components of these flows by using a combination of surface height anomalies measured from satellite altimetry and in situ data on the baroclinic field. While this problem might be considered in any of the western boundary currents, for example, the Kuroshio-Oyashio or the Gulf Stream-Slope Water regime, we concentrate our analysis on the Brazil-Malvinas Confluence. This regime is characterized by a weak, warm southward Brazil Current (BC) meeting a strong, cold, less saline northward current, the Malvinas (Falkland) Current (MC). The MC is a branch of the Antarctic Circumpolar Current, which has large barotropic components.

In this work we define the currents as the flows above the pycnocline. This definition of the currents, while leading to quantitative transports results here, only partially addresses the debate in the literature over the structure of these two currents. Various authors [Gordon, 1989; Roden, 1986; Gordon and Greengrove, 1986] investigate the contrasts in water masses in the confluence, which we do not discuss in detail here. Rather, we emphasize the dynamics in the upper layer of the confluence in terms of the vertical structure typical of the Subantarctic front and the edge of the subtropical gyre.

Our goal in this work is to provide a method that uses satellite altimetry to estimate the thickness of the upper layer of the ocean, which goes from the surface to the depth of the 8°C isotherm, and the transport within that layer in a region characterized by the presence of a western boundary current. To accomplish this, we combine in situ data from two data sets, one provided by an array of inverted echo sounders (IES) [Confluence Principal Investigators, 1991], and another from the Geosat Exact Repeat Mission (ERM) passes over the confluence region. The nature of these two data sets limits the ability of the analysis to address the structure of the deep flows. Nevertheless, we use them to quantify the baroclinic and baro-

Copyright 1996 by the American Geophysical Union.

Paper number 96JC01146.  
0148-0227/96/96JC-01146\$09.00

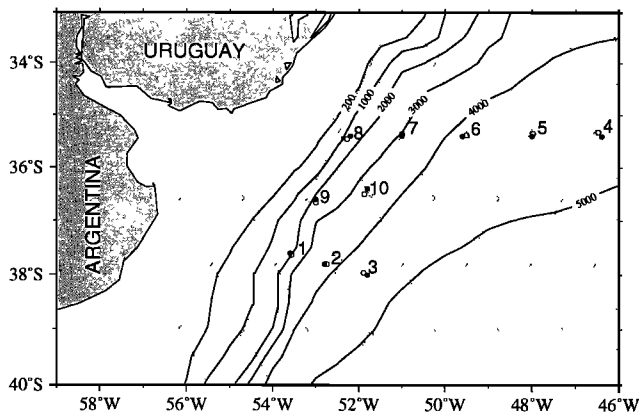


**Figure 1.** Locations of the deployment of the 10 inverted echo sounders (IESs, solid circles) and the Geosat altimeter grid positions (open circles) off the Argentine continental shelf. The bathymetry, with depths in meters, and the Geosat Exact Repeat Mission (ERM) ground tracks (dotted lines) are included in the figure.

tropic contributions to the upper layer boundary current flows. We also utilize satellite infrared imagery to help identify frontal positions and surface mesoscale features. This work is an extension of the various mappings of boundary currents using altimeter-derived sea height anomalies [Cheney *et al.*, 1983; Kelly, 1991; Kelly *et al.*, 1991; Kelly and Gille, 1990] to include a decomposition between the baroclinic and barotropic modes. This effort to combine IES and altimeter data extends earlier comparative analyses of these sorts of data in the Gulf Stream by Hallock and Teague [1993] and Teague *et al.* [1995]. This type of analysis is especially valuable in the confluence region because of the debate over the structure of the two currents that in particular makes the specification of the two currents' transports uncertain [Gordon, 1989; Zemba, 1991; Peterson and Stramma, 1992; Smith *et al.*, 1994]. Again, the definition of the two currents used here is limited to the surface flows as defined by the pycnoclines. In this respect the fine-scale issues of the North Atlantic Deep Water and Antarctic Bottom Water flows cannot be addressed within the error bars.

There exist several descriptions of the dynamics of the Brazil and Malvinas Currents, along with their confluence. One of the earliest data sets describing these currents' paths is the sea surface thermal front mapping by Legeckis and Gordon [1982]. The separation of the currents from the continental shelf over time is analyzed quantitatively by Olson *et al.* [1988] and Matano [1993]. More recent works compare data on frontal positions with IES-derived current positions [Garzoli and Bianchi, 1987; Garzoli and Garraffo, 1989; Garzoli and Simionato, 1990]. Garzoli [1993] uses an IES data set to estimate 0/1000 dbar transports and their relationship to wind forcing. Altimeter-based descriptions of the confluence region include the rms surface height charts by Cheney *et al.* [1983], a mapping of sea height anomaly (SHA) distributions versus sea surface frontal positions by Provost *et al.* [1989], and studies of temporal variations over time by Provost and Le Traon [1993] and Forbes *et al.* [1993]. Garraffo *et al.* [1992] use the combination of data sets, including Geosat altimetry, to consider the validity of the Semtner and Chervin [1992] global eddy-admitting circulation model. Finally, there are several model studies of the confluence and its variability in relationship to various forcing

sources [Garzoli and Simionato, 1990; Matano, 1993; Campos and Olson, 1991; Smith *et al.*, 1994].

We begin this work with a brief introduction of the Geosat and IES data sets and advanced very high resolution radiometer (AVHRR) images used in this study. We follow with a description of the changes in sea height and thickness of the upper layer caused by the passage of the BC front, the MC, and warm (anticyclonic) and cold (cyclonic) eddies. We continue with a theoretical discussion of the diagnostic two-layer ocean model we use to decompose the circulation into baroclinic and barotropic contributions. We examine the relationship between sea height and upper layer thickness changes caused at each IES site by the passage of a front or a mesoscale feature, which allows us to estimate the reduced gravity in the area. We later introduce a method based on this model to monitor the thickness of the upper layer using altimeter data. We also propose two methods to estimate the mean barotropic sea height change in the region, one based on the conservation of mass and another on the conservation of potential vorticity. Finally, we round out this work by computing the time series for upper layer thickness difference and the barotropic and baroclinic transports between two selected IES sites for the entire Geosat ERM time period.

## 2. Data Sources

### 2.1. Inverted Echo Sounders

Inverted echo sounders are devices placed on the bottom of the ocean to simultaneously work as a sound source and receiver. They register the time that an acoustic signal takes to reflect at the sea surface and return to the bottom of the ocean. These travel times are regressed against hydrographic data to find an algorithm for computing the dynamic height and the thickness of the upper layer, which goes from the free surface to the thermocline depth [Watts and Rossby, 1977; Garzoli and Garraffo, 1989].

In the first study of its kind in the SW Atlantic Ocean, two consecutive experiments were carried out with two and three IESs deployed between November 1984 and April 1986. Garzoli and Bianchi [1987] use the data from the first experiment (November 1984 to June 1985) to study the BC front oscillations and to estimate the southward transport across 37°50'S in the upper 800 m. They estimate a mean BC transport of 10 Sv ( $1 \text{ Sv} = 10^6 \text{ m}^3 \text{ s}^{-1}$ ), with peaks of around 23 Sv. In the second experiment, three IESs were deployed between June 1985 and March 1986. Garzoli and Garraffo [1989] use this data to estimate the transport relative to 800 m at around 11 Sv for the BC and 3.5 Sv for the MC. Additionally, they identify an annual oscillation in the location of the BC front. Garzoli and Simionato [1990] also use these data to study baroclinic instabilities as well as the wind-driven frontal oscillations of the BC.

In a third experiment, 10 IESs were deployed in the Brazil-Malvinas Confluence region from November 1988 to February 1990 [Confluence Principal Investigators, 1991]. These data are the basis of Garzoli's [1993] transport estimates. We use the data provided by this array of 10 IESs placed off the Argentine continental shelf between 35° and 38°S, at locations depicted by solid circles in Figure 1. The dotted lines in the same figure represent the Geosat ERM ground tracks. Table 1 shows the locations and depth for each of the IES sites. We analyze the errors in a way similar to that described by Garzoli and Bianchi [1987]. We regress the conductivity-temperature-depth (CTD) data collected during cruises to the data collected at the 10 IES

sites to obtain a relationship between changes in travel time and changes in the depth of the 8°C isotherm,  $h_1$ . We compute the 8°C isotherm and the travel time, defined as the integral of the inverse of the sound velocity, for every CTD cast. We then obtain a regression between both quantities with an error of the estimate of 16 m, with a correlation coefficient of 0.9. We finally adjust the time series of  $\Delta h_1$ , where  $\Delta h_1 = h_1 - \bar{h}_1$  and  $\bar{h}_1$  is the time average of the series, to the values measured during the cruises to obtain the values of  $h_1$ .

## 2.2. Geosat Altimeter

We use the Geosat ERM T2 geophysical data records (GDRs), so called because the orbits are based on the Goddard Earth Model T2 [Haines *et al.*, 1990], to compute the values of SHA in the SW Atlantic Ocean. We apply corrections to the data set similar to those described in detail by Cheney *et al.* [1987], which include solid and ocean tides and wet and dry tropospheric, ionospheric, EM bias, and inverse barometric corrections. We then interpolate the corrected heights onto a 7-km along-track grid and compute a mean or reference sea surface profile for each track using a slightly modified collinear approach similar to that proposed by Chelton *et al.* [1990]. This method estimates the mean sea height from the mean along-track slope of interpolated sea heights at fixed grid points in a process equivalent to integration, i.e., by reconstructing the curve from its mean slope value at each grid point. We find that there is not a repeated occurrence of missing data, which usually causes differences between the arithmetic mean and the reference profiles. We then compute the SHA at each grid point and every cycle by subtracting the reference estimate from the sea height values. This last step also eliminates the time-invariant orbit error. We use only the SHA, as the absolute sea surface topography cannot be estimated from the currently available geoid model. Finally, we estimate and remove the time-dependent orbit error from the signal by fitting a sinusoid to each cycle. We take extreme caution when comparing SHA values from different sites with one another, since they are referred to different mean values. However, at a fixed site, changes in SHA are the same as changes in sea height. We use this concept in the following sections when we give both variables the same meaning.

The 10 IES locations were chosen to lie close to the Geosat ERM ground tracks to better blend with altimeter data. Since the Geosat altimeter provided data until September 1989, we can use only the combined Geosat altimeter and IES data corresponding to the period November 1988 through Septem-

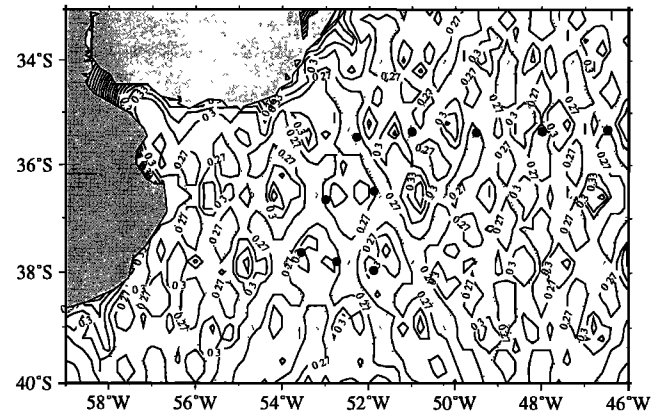


**Figure 2.** Map of normalized error for the objective-analysis-derived sea height anomaly (SHA) field in the SW Atlantic Ocean, corresponding to the period February 11–15, 1988. The estimation variances range from 0.25 to 0.33 times the field of variance. The smallest errors occur along the Geosat ERM ground tracks (dotted lines), while the largest are in the areas distant from them. The solid circles correspond to the IES sites.

ber 1989, referred to from now on as the study period. In order to estimate the SHA values as close as possible to the IES locations and to account for the mesoscale features present in the area, we use the objective analysis (OA) scheme described by Mariano and Brown [1992] to interpolate the SHA into a 0.2° grid every 5 days. The last two columns in Table 1 show the grid locations closest to the IES site which we use to extract the values of SHA. The solid circles in Figure 1 indicate the IES sites, while the open circles show the grid locations of the OA-derived SHA. Figure 2 shows a typical map of normalized errors, corresponding to the period February 11–15, 1988. We define these errors as the estimation variance divided by the field variance, obtained for the OA computations. The dotted lines in the same figure show the Geosat ERM ground tracks. The mapping estimation variances are a function of the correlation matrix and data locations. The minimum estimation variances of around 0.25 times the field variance occur along the altimeter ground tracks. The maximum estimation variances of around 0.33 times the field of variance occur in areas distant from the ground tracks.

## 2.3. AVHRR Images

We make use of 5-day sea surface temperature (SST) composites constructed from AVHRR images available for this region [Podesta *et al.*, 1991]. These composites provide information on the sea surface thermal contrast, and we use them as a guide to identify mesoscale surface features and frontal movements. However, this is not always possible as the images present many gaps during the southern hemisphere winter due to the constant presence of clouds. We extract the SST values from AVHRR composites, and as they only provide a measure of the temperature from the upper millimeters of the sea surface, they do not always show a correspondence with the SHA and the thickness of the upper layer. The location of the boundaries of the MC and cold eddies are not always easily distinguishable at the surface, since a thin warm layer of water can cover these features.

**Table 1.** Locations of the 10 Inverted Echo Sounder (IES) Deployments, the Ocean Depth at Their Sites, and the Locations Used for the Geosat Objective Analysis (OA)

IES Site	Depth, m	IES Latitude	IES Longitude	OA Latitude	OA Longitude
1	2852	37°37'S	53°34'W	37°36'S	53°36'W
2	3804	37°48'S	52°45'W	37°48'S	52°48'W
3	4346	37°57'S	51°53'W	38°00'S	51°48'W
4	4824	35°19'S	46°29'W	35°24'S	46°24'W
5	4688	35°21'S	47°59'W	35°24'S	48°00'W
6	4247	35°22'S	49°30'W	35°24'S	49°36'W
7	3018	35°21'S	51°00'W	35°24'S	51°00'W
8	1327	35°27'S	52°16'W	35°24'S	52°12'W
9	2231	36°39'S	53°00'W	36°36'S	53°00'W
10	3307	36°29'S	51°52'W	36°24'S	51°48'W

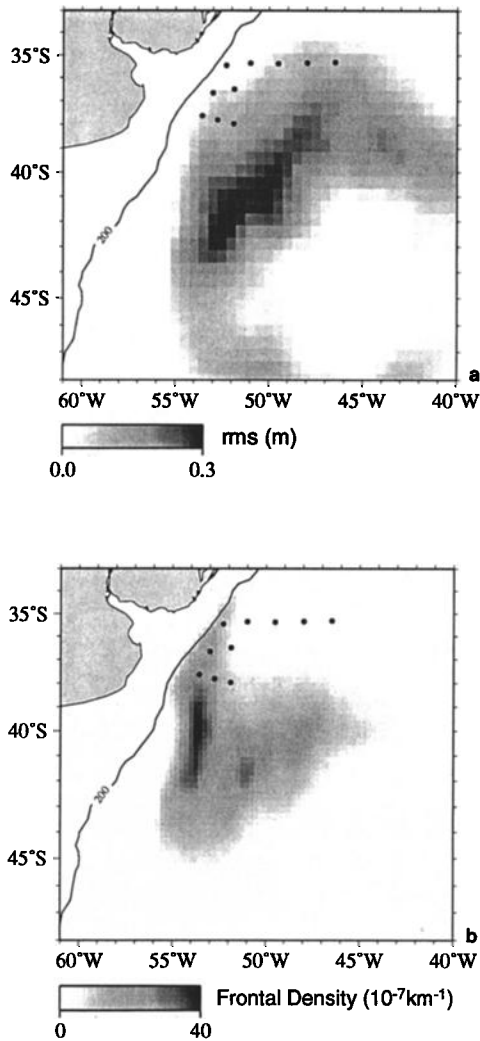


**Figure 3.** (a) Root-mean-square variability, in meters, of the sea surface height field in the SW Atlantic Ocean, as obtained from Geosat data from November 1986 to September 1989. Higher values of around 0.30 m are found in the Brazil-Malvinas Confluence region and are associated with the presence of frontal movements and mesoscale processes. (b) Frontal density fields, in  $10^{-7} \text{ km}^{-1}$ , computed following the method proposed by *Garzoli et al.* [1992] using AVHRR-derived Brazil Current frontal positions from 1984 to 1989. The higher values along  $54^{\circ}\text{W}$  denote a preferred position for the fronts off the continental shelf before they retroflect to the NE direction. The circles in both figures show the location of the 10 IES sites, and the solid line indicates the 200-m isobath. We show the actual values of rms variability and FD at each IES site in Table 2.

### 3. Mesoscale Features and Frontal Movements

Many studies analyze the circulation in the Gulf Stream and/or Kuroshio regions using only altimeter data [*Tai*, 1990; *Kelly*, 1991; *Kelly et al.*, 1991; *Qiu*, 1992]. These works provide a methodology to estimate the transports across the Geosat ERM ground tracks in these regions based on synthetically derived mean sea height profiles. *Ezer et al.* [1993] assimilate Geosat altimeter and synoptic SST data into a numerical model of the Gulf Stream region to analyze the dynamics of the mesoscale features in that area. Most of the studies focusing on the relationship between the sea surface topography and

the subsurface thermal structure in frontal areas are also limited to the Gulf Stream and Kuroshio regions. *Szcechowski* [1992] conducted a study combining Geosat and air-dropped expendable bathythermograph (AXBT) data, in which the surface thermal front is usually displaced to the north of the subsurface front, which in turn is generally located to the south of the Geosat-derived frontal position. Published literature on the combination of two or more remote-sensing methods to study the dynamics of western boundary currents is more scarce. *Hallock and Teague* [1993] and *Teague et al.* [1995] study the correlation of sea surface height anomalies measured by IESs and compare them with Geosat and TOPEX/POSEIDON altimeter data, respectively. We are not aware of any study that simultaneously combines altimetry and other remote-sensing-derived data to study the upper layer circulation in the SW Atlantic Ocean.

#### 3.1. Variability in the Brazil-Malvinas Confluence Region

The Brazil Current separates from the continental slope at around  $37^{\circ}\text{S}$  and then begins meandering, turning first to the SE and then to the NE, with fluctuations geographically limited by the continental slope to the west and around  $49^{\circ}\text{S}$  to the south. We identify the BC surface front using AVHRR 5-day composites at the location of the maximum SST gradient in the area where the jet of the BC encounters the waters of the MC. From altimeter data we approximate the location of the BC axis at the position of the maximum along-track SHA gradient, going from south to north, in the area close to the thermal front. The jet of the BC and the surface thermal front are positioned at different locations, with the thermal front usually located to the south of the jet of the current. However, owing to the presence of complicated patterns of currents, counter-currents, eddies, and meanders, this situation is sometimes reversed.

We illustrate the complexity of the region's dynamics by means of two types of maps: (1) a map with the spatial SHA variability in the region constructed from GEOSAT altimeter data (Figure 3a) and (2) a frontal density (FD) map derived from BC surface fronts using AVHRR composites (Figure 3b), with the FD being a measure of the probability of finding the surface thermal front [*Garzoli et al.*, 1992].

Figure 3a shows the rms SHA values from November 1986 to September 1989, the period of time covered by the Geosat ERM. The rms sea height anomaly has the same value as the rms sea height because the anomalies are referred to a curve that approximately represents the arithmetic mean. The spatial average of the rms sea height anomaly values for the confluence area is around 0.15 m, with maximum values of around 0.35 m. Going from north to south through the confluence region, the rms sea height anomaly increases until it reaches its peak value, exhibiting afterward a rapid decrease. We speculate that this situation arises from the fact that the BC fronts generally have a smaller (higher) sea height change to the north (south) of the highest rms sea height values. *Provost et al.* [1989] report a similar result for a study of the variability of the dynamic height relative to 1400 m in the same area, with the smallest variability values in the south of the confluence region.

Figure 3b shows the surface FD values (in reciprocal kilometers) between July 1984 and February 1989, computed using the method described by *Garzoli et al.* [1992]. The higher FD values along the continental slope, at approximately  $54^{\circ}\text{W}$ , north of the BC retroflection imply a rather small EW oscillation. After the BC turns to the NE, the range of the oscillation

**Table 2.** Geosat-Derived Root-Mean-Square Sea Height Variability, AVHRR-Derived Frontal Density (FD), and IES-Derived Values of the Mean and Standard Deviation for Upper Layer Thickness at Each of the 10 IES Sites and for the 10 Sites Together

IES Site <i>i</i>	rms, m	FD, $10^{-7} \text{ km}^{-1}$	Mean $\bar{h}_{1,i}$ , m	$\sigma$ , m
1	0.16	20	133	110
2	0.18	8	322	189
3	0.20	6	519	153
4	0.18		456	105
5	0.18		444	130
6	0.16		550	114
7	0.12		668	60
8	0.11	14	456	75
9	0.15	19	297	187
10	0.16		585	102
All	...	...	443	196

Blank entries in the FD column indicate values of less than 1.

tions in the latitudinal and longitudinal directions is larger, as is represented by smaller FD values dispersed over a wider area. When the frontal movements are restricted to a very small region, the areas with high FD values also have relatively small rms SHA values. However, this situation does not occur in the confluence region, where the BC fronts are located over an area of around  $10^6 \text{ km}^2$ . We note that west of  $54^\circ\text{W}$  the higher rms values are located to the east of the higher FD values, which implies larger variations of sea height toward the center of the subtropical gyre, due to more intense meander and eddy activity.

The 10 IESs are located in an area of different characteristics in their dynamics, where the rms SHA values range from 0.11 to 0.20 m, and the FD values extend from 0 to  $20 \times 10^{-7} \text{ km}^{-1}$ . Table 2 shows the rms and FD values at each IES site. We observe that sites 2 and 3 are located in an area of high rms sea height variability and high FD values. Sites 4, 5, 6, and 10 are located in an area of high rms sea height variability and low FD values. Site 7 is located in an area of low rms sea height variability and low FD values, and sites 1, 8, and 9 are located in an area of low rms sea height variability and high FD values. Although the IESs are not located in the areas with the highest rms and FD values, they are positioned across the jet of the BC current, which is especially important for transport computations. We also consider it noteworthy that the higher rms values are not usually associated with preferred frontal locations.

### 3.2. Sea Surface Temperature, Upper Layer Thickness, and Sea Height Anomaly

Figure 7 illustrates the geometry of the vertical structure showing the upper layer thickness and SHA. Figure 4 shows the time series of the upper layer thickness as obtained from the IESs, the SHA from the Geosat altimeter data, and the SST from AVHRR composites, at each of the 10 IES sites. We show the correspondence between these parameters and the lines in the top right panel of the figure. We filter the values of the SST and upper layer thickness time series with a Hanning filter to exclude high-frequency variations of less than 20 days. We then subsample the SST and upper layer thickness time series for 5-day intervals for the approximately 11-month length of the study period, thus obtaining 66 data points for each of the time series. In this section we investigate simulta-

neous changes in SHA, upper layer thickness, and SST associated with the movements of the BC, MC, and mesoscale features. After we analyze these changes, we locate several significant surface features, three eddies and two surface fronts, and explore in more detail the effect of these events on the SHA and the upper layer thickness.

The SST has an annual cycle with maximum values during the summer months of the southern hemisphere, i.e., December through March, which becomes more noticeable in areas close to the continental shelf [Podesta *et al.*, 1991], as seen in sites 1, 8, and 9. Site 1 shows the minimum SST value of  $8.0^\circ\text{C}$  during the month of June. This site also shows higher fluctuations of SST due to the presence of the MC and BC water masses on the surface at different times. The maximum value of SST, around  $25.0^\circ\text{C}$ , occurs during the end of summer at site 8, which is usually crossed by the core of the BC. The time of the year when this occurs suggests a nonseasonal SST variability, related to the oscillations of the BC and MC, which agrees with the results obtained by Podesta *et al.* [1991]. The AVHRR composites reveal that the influence of the MC surface intrusion to the north is more noticeable from May through July at site 1 and during August at site 9. This northern intrusion of the MC causes the BC front to separate from the continental slope at around  $34^\circ\text{S}$ , somewhat to the north of the previous reported value of  $35^\circ\text{S}$  for a different period of time [Olson *et al.*, 1985].

The time series in Figure 4 that corresponds to IES 1 shows the surface features responsible for the largest changes in upper layer thickness. A warm eddy (W) crosses this site in November, causing a rise in SHA and an increase in the upper layer thickness. The BC front crosses site 1 in January (BC), and the jet of the BC passes through this same site in February and July (BJ), producing similar effects on the SHA and upper layer thickness. The MC front passes through site 1 in February, March, and April (MC), causing the thermocline to rise and the SHA to decrease. The Subantarctic waters (S) cover this site in May and June, causing the thermocline to rise to the surface. The correspondence between the SHA and upper layer thickness at each IES site is easily visualized in Figure 4, in which an increase in the thickness of the upper layer is usually associated with a rise in the sea height. However, we also notice that for each pair of SHA and upper layer thickness values, the best agreements do not appear to be correlated with events associated with larger amplitudes.

The thermocline rises to the surface only at site 1, during the months of May and June 1989, owing to the presence of the MC on the surface at this location. However, we notice that the SST for this period of time is not  $8^\circ\text{C}$ , the value assigned in this work for the thermocline. This can be explained because the SST, as found from the AVHRR composites, is only a measure of the skin temperature of the ocean [Schluessel *et al.*, 1987] and also because the  $8^\circ\text{C}$  isotherm depth obtained from the IESs is an estimate based on regressions using hydrographic data. The upper layer thickness gets its largest values, of more than 700 m, in the offshore locations, at site 3 for the months of January and March and site 7 for the month of June.

In general, the movement of the BC front causes an increase of up to 700 m in the upper layer thickness, due to a change in regime from Brazil waters to Malvinas waters. These values are from 2 to 4 times larger than the upper layer thickness increase caused by the passage of warm eddies in this region, which is of approximately 200 m. The largest changes in the thickness of the upper layer occur during periods ranging from 1 to 3

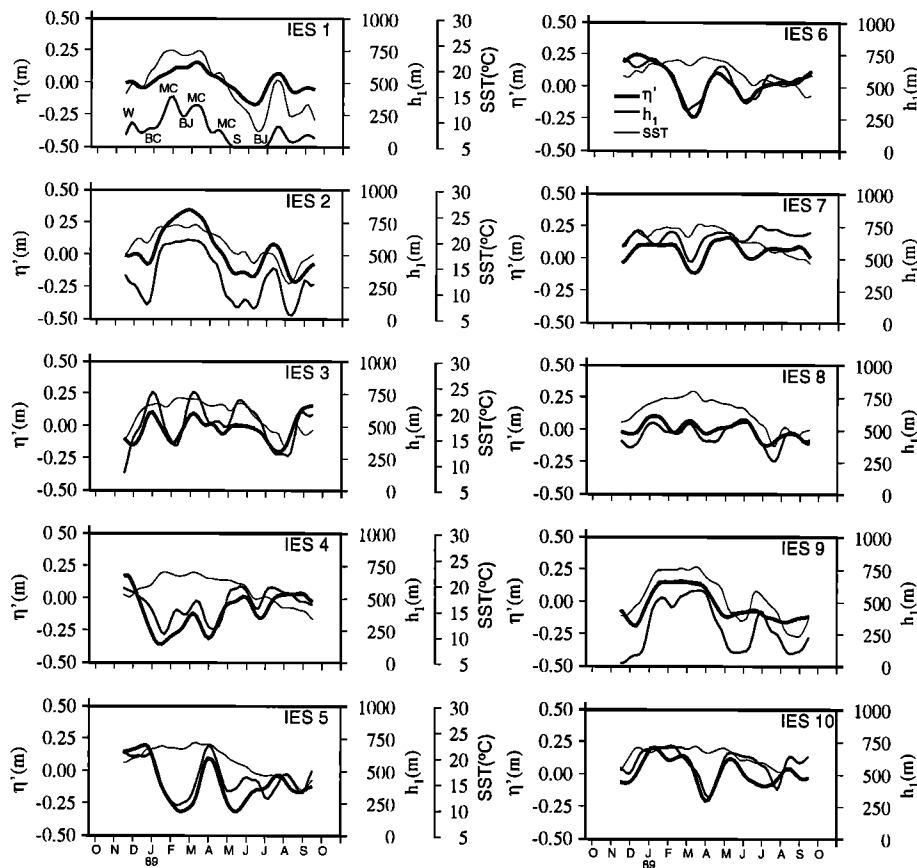


**Figure 4.** Time series for the sea surface temperature (SST, degrees Celsius), sea height anomaly  $\eta'$  (meters), and upper layer thickness  $h_1$  (meters) for IES sites 1 through 10. The correspondence between these parameters and the lines is shown in the top right panel. The time interval goes from October 1988 through October 1989. Several important surface features are included in the top left panel that corresponds to IES 1; the abbreviations correspond to the passage of a warm eddy in November (W), the BC front in January (BC), the jet of the BC in February and July (BJ), the MC front in February, March, April, and May (MC), and the Subantarctic waters (S) in May and June.

months in sites located on the east side of the array, with increases of more than 500 m in 3 months.

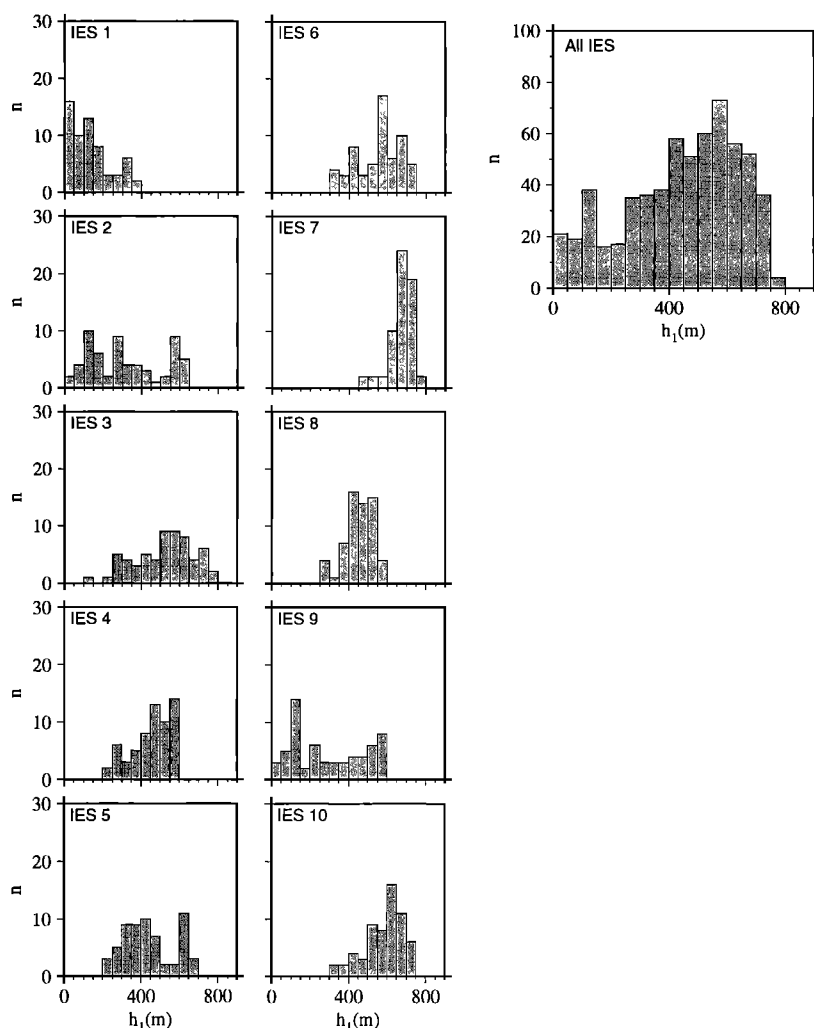
Figure 4 reveals that the rise of the sea surface height after the passage of the BC front ranges approximately from 0.10 to 0.40 m, with an average of 0.30 m and with the largest values corresponding to the offshore sites. Changes in SHA of around 0.40 m are observed at every site except for site 8, which has the lowest SHA rms values, of around 0.10 m. Sea height variations associated to the passage of the BC front are from 2 to 3 times greater than those resulting from the passage of an eddy. On the other hand, upper-layer thickness variations associated with the passage of the BC are from 2 to 4 times larger than those resulting from the passage of an eddy.

Figure 5 shows the frequency distribution of the thickness of the upper layer at each of the 10 sites (small panels), and for the 10 sites together (large panel). The mean and standard deviation values are shown in Table 2. We find the largest values of upper layer thickness and lower standard deviation values at sites 3, 6, 7, and 10, which are the locations frequently crossed by the jet of the BC. It is difficult to associate any of the distribution patterns in Figure 5 with a Gaussian distribution. However, we observe an approximate Gaussian distribution at sites 6, 7, 8, and 10, which are sites that are mostly in BC waters. The rest of the sites present patterns that are defini-

tively not Gaussian because of the change from BC to MC regimes. *Kim and Rossby [1979]* examine variations in thermocline depth after the passage of a front or an eddy in an area of the North Atlantic Ocean, concluding that different statistics, one for eddies and another for the mesoscale field, must be used to describe the variability. They also concluded that the formation of eddies can therefore be associated with the tails in the histograms. Our data show that this effect is sometimes strong enough to generate a multimodal structure, as can be seen in sites 2, 5, and 9. A tail toward the right, with thicknesses of the upper layer larger than the mean, can be seen at site 1, the westernmost IES site. This large number of small upper layer thicknesses is due to the presence of the MC at or close to the surface. Some sites (3, 6, and 10) present a tail to the left, with upper layer thicknesses smaller than the mean, owing to the presence of warm core eddies.

### 3.3. Selected Mesoscale Features and Frontal Movements

*Garzoli [1993]* analyzes some of the mesoscale and frontal features present during the study period, as well as some aspects of the variability and intensity of the flows in the region. This work also provides an overview of the cyclonic and anticyclonic circulations as well as the northern penetration of the MC and the separation of the Brazil Current from the conti-



**Figure 5.** Histograms of distribution of the upper layer thickness  $h_1$ , for each of the IES sites (small panels) and for the 10 sites together (large panel). The mean and standard deviation values for each site are shown in Table 2.

mental shelf. In this section we expand the discussion provided by *Garzoli* [1993] to include the simultaneous changes in the thickness of the upper layer, sea surface height, and sea surface temperature in three eddies and two frontal movements.

The AVHRR composites show that during the study period the largest cold and warm eddies are formed south of  $38^\circ\text{S}$ , that is, south of the area covered by the IESs. However, we still identify two warm eddies in surface water during November 1988 (Figure 6a) and June–July 1989 (Figure 6b) north of  $38^\circ\text{S}$ . These warm core eddies are formed when a portion of a BC meander pinches off an anticyclonic vortex into colder Subantarctic waters. These two eddies are rather uncommon, since they are formed on the western boundary of the BC and very close to the continental slope. Their trajectory is almost decided at that point, because they never cross the continental slope to the west and, at the same time, the MC pushes them to the NE, making them rejoin the BC or simply disappear [*Legeckis and Gordon, 1982*]. *Legeckis and Gordon* [1982] also report that cold eddies, made up of Subantarctic MC waters, are more frequently found between  $40^\circ$  and  $50^\circ\text{S}$ . However, we find a cold eddy at approximately  $36^\circ\text{S}$  during the month of July–August 1989 (Figure 6c). Although we observe both cold and warm eddies in the area of study, we do not generalize the

following analysis for areas south of  $38^\circ\text{S}$ , as the sea height variations across the BC fronts increase as the fronts move toward the south.

A warm eddy, eddy A, begins forming between sites 9 and 10 during mid-November 1988, the beginning of the IES experiment. On November 22 this small eddy appears well formed, with its center to the SE of site 1. Figure 6a shows the thermal field extracted from the SST composite corresponding to November 20–24, Eddy A is highly elliptical, oriented meridionally, and, from the AVHRR composite, does not show a very well defined southern limit at the surface. Its major axis is nearly 400 km, and its minor axis is about 60 km. The surface temperature of the core of eddy A is about  $19.3^\circ\text{C}$ , with surrounding waters of  $14.0^\circ\text{C}$  to the west and  $15.3^\circ\text{C}$  to the east. Eddy A shows a relatively short life of around 15 days, as the SST composites reveal that it joins the main jet of the BC again by the beginning of December. During this short period of time, eddy A causes a rise in sea height of about 0.30 m and an increase in the thickness of the upper layer of only 30 m. Even though eddy A is rather superficial in nature, it is very well detected by Geosat. Figure 6a has superimposed the Geosat ground track that crosses this eddy. Next to this figure we show the SHA along the Geosat track for November 26. We observe

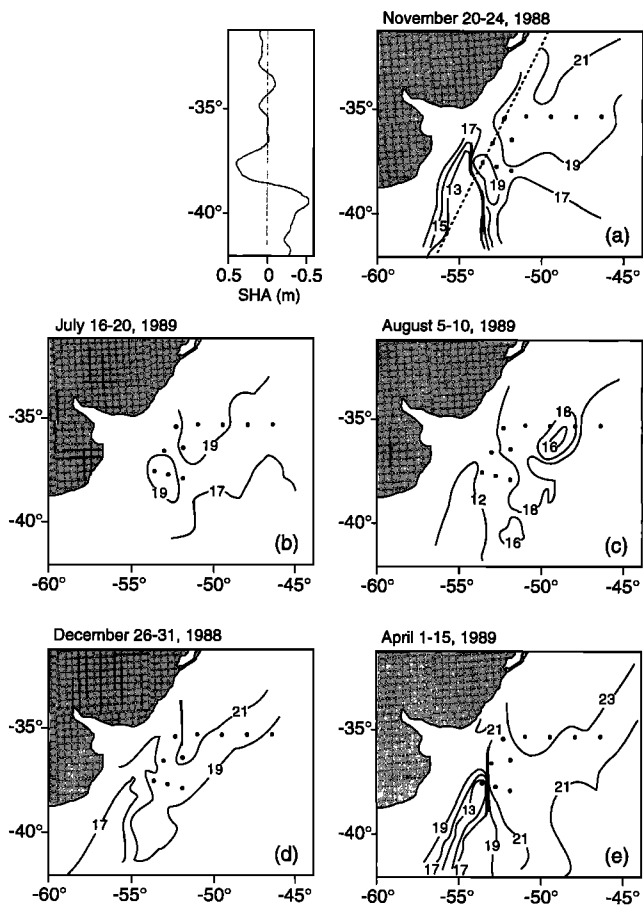


**Figure 6.** Sea surface temperature diagrams obtained from AVHRR-derived 5- or 10-day composites showing (a) a warm eddy, eddy A, formed in November 1988; (b) a warm eddy, eddy B, formed in June 1989; (c) a cold eddy, eddy C, formed in July 1989; (d) the Brazil Current front moving from west to east in December 1988; and (e) the Malvinas Current front moving toward the east in March 1989. Figure 6a also has superimposed a Geosat ERM ground track. The altimeter-derived SHA profile that corresponds to November 26, 1988, is shown to the left of the figure; the warm eddy appears as positive values in the profile.

the correspondence between sea height and the dynamics of the surface processes as we go south along the Geosat track. The SHA values decrease when the track passes from the warm BC waters to the MC waters. We can identify eddy A as a positive SHA, with a peak value of around 0.30 m, in the SHA profile of Figure 6a.

A better defined eddy on the surface, eddy B, forms in June 1989 in the area covered by sites 1, 2, and 9. By the end of June the BC front crosses the locations corresponding to sites 9 and 2, and shortly after this, eddy B begins to form. By the beginning of July it grows and translates slightly to the west to also cover site 1. By July 15 this warm eddy is already well defined at the surface, with its center located at 38°S and 53°W, its western boundary close to site 1, and its eastern border close to site 2. Figure 6b shows a map with a diagram of the SST conditions in the area during July 16–20. The SST of the core of eddy B is around 20.1°C; the temperature of the surrounding water is 9.1° and 16.2°C to the west and east of the eddy, respectively. As in the case of eddy A, the temperature to the west of the eddy is colder than the temperature to the east,

owing to the presence at the surface of MC waters. Eddy B is clearly identified in the SST time series for sites 1 and 2, with peak SST values of around 20°C during the month of July (Figure 4, sites 1 and 2). From the SST composites we estimate the longitudinal and latitudinal surface axes of eddy B to be about 124 km and 200 km, respectively. The formation of eddy B lasts for approximately 1 month. After it is formed, eddy B rapidly disappears from the SST composites and is gone by June 25, 5 days after it is completely formed. During this month the thermocline lowers from 0 m to 200 m depth in site 1, and from 50 m to 400 m in site 2. The passage of eddy B also causes a sea height rise at these two IES locations of about 0.20 m.

The BC front moves to lower latitudes during the winter months than during any other season. From the AVHRR composites we observe Subantarctic waters from the MC on the surface at latitudes as far north as 32°S off the coast of Brazil during the winter [Garzoli *et al.*, 1992]. A cold eddy, eddy C, begins forming from a surface intrusion of cold Subantarctic water at 36°S at the beginning of July 1989. Figure 6c shows the SST conditions in the area for the period August 5–10. The eastern border of eddy C is located at site 5 at the beginning of August. The temperature at the core of this eddy is about 15.1°C, with surrounding SST of around 18.9°C. The axis at the surface is about 188 km longitudinally and 218 km latitudinally. During this month the thickness of the upper layer increases from 500 to 300 m, and the sea surface lowers 0.20 m. We cannot estimate the life span of this eddy owing to cloud coverage in the SST composites. However, we notice that it finally joins the rest of the colder water that covers the area during the month of August.

We observe that the passage of the BC causes the largest variations in thickness of the upper layer and sea height. We examine a zonal movement of the BC front from west to east during the months of November and December 1988, as detected at site 9. We show in Figure 6d the SST conditions for December 26–31, 1988. Figure 4 shows that the passage of the front at site 9 produces an increase in the thickness of the upper layer of around 600 m and a rise of the sea height of around 0.35 m over a 2-month period.

By mid-March 1989 the MC front moves toward the north along the continental slope, crossing site 1 from west to east. We show in Figure 6e the SST conditions for April 1–April 15. The waters of the MC stay in this area until the month of June. We see in Figure 4 that during this period of time the thermocline rises from 350 m to 0 m, and the sea height drops 0.40 m.

## 4. Decomposition of the Vertical Structure With Thermocline Depth and Sea Height Anomaly

### 4.1. Two-Layer Model

Figure 7 shows the assumed geometry, in which we use the common two-layer approximation of the vertical structure of the ocean to describe the sharp vertical gradient that surfaces near surface and deep waters in the Brazil-Malvinas Confluence [Gordon, 1989]. We treat the system as having thermocline deviations and a reduced gravity that produce pressure gradients associated with the baroclinic structure of the circulation. We choose the thermocline to correspond to the 8°C isotherm. The reduced gravity is  $g'$ , where  $g' = g(\rho_2 - \rho_1)/\rho_2$ ,  $g$  is the gravitational acceleration, and  $\rho_1$  and  $\rho_2$  are

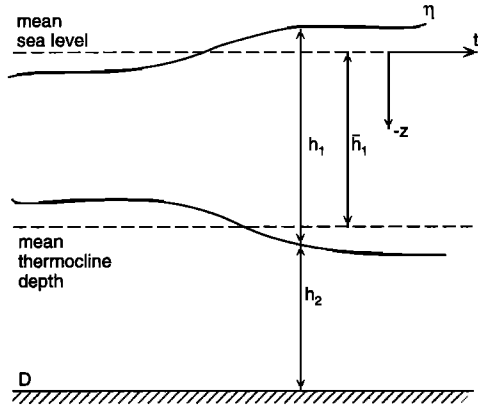


**Figure 7.** The approximate geometry of the Brazil-Malvinas Confluence region where the 10 IESs were deployed. The horizontal axis is the time  $t$ ; an increment in the upper layer thickness  $h_1$  corresponds to a rise in the sea height elevation  $\eta$ .  $\bar{h}_1$  is the mean upper layer thickness; the ocean depth is  $D$ , and the upper layer thickness anomaly is  $h_1'(t) = h_1(t) - \bar{h}_1$ .

the densities of the upper and lower layers, respectively. We also assume the lower layer to be in motion and tied to a vertically constant barotropic component of the horizontal pressure gradient in both layers. We then need to specify the contribution of the two pressure gradients, baroclinic and barotropic, to the sea surface height observed from the altimeter.

The ocean has a total fluid column depth  $D(x)$ , from a surface that is assumed to correspond to the geopotential surface if the ocean is at rest. The variable  $x$  is a one-dimensional horizontal coordinate. The water column is divided into upper and lower layers with thicknesses and densities of  $h_1(x, t)$ ,  $\rho_1$ , and  $h_2(x, t)$ ,  $\rho_2$ , respectively. The sea height is then

$$\eta(x, t) = h_1(x, t) + h_2(x, t) - D(x). \quad (1)$$

At a fixed location the sea height is then

$$\eta(t) = h_1(t) + h_2(t) - D. \quad (2)$$

If we ignore the pressure variations in the atmosphere, we can write the pressure distribution in both layers as

$$\begin{aligned} P_1(t) &= \rho_1 g [h_1(t) + h_2(t) - (D + z)], \\ P_2(t) &= \rho_1 g h_1(t) + \rho_2 g [h_2(t) - D - z]. \end{aligned} \quad (3)$$

We can then write the pressure gradients in terms of a baroclinic component that is proportional to  $h_1'(t)$ , and a barotropic contribution to the pressure field. We recognize the latter in terms of the temporal portion of the lower layer pressure. We obtain this by rewriting the lower layer pressure as

$$P_2(t) = \rho_2 g \left[ \frac{\rho_1}{\rho_2} h_1(t) + h_2(t) - D - z \right]. \quad (4)$$

Noting that  $D + z$  adds no horizontal variations in the fluid column, the barotropic component becomes

$$B(t) = \rho_1 / \rho_2 h_1(t) + h_2(t) - D. \quad (5)$$

We rewrite the sea height (equation (1)) as a function of a baroclinic and barotropic component:

$$\eta(t) = \varepsilon h_1(t) + B(t), \quad (6)$$

where

$$\varepsilon = (\rho_2 - \rho_1) / \rho_2. \quad (7)$$

Equation (6) shows the decomposition of the sea height into a baroclinic ( $\varepsilon h_1$ ) and a barotropic ( $B$ ) component.

If  $\eta'$  is the sea height anomaly, or departure of the sea height from the mean or reference sea height ( $z = 0$ ), we can write to a first approximation

$$\bar{\eta} = \varepsilon \bar{h}_1 + \bar{B} = \varepsilon \bar{h}_1 \left( 1 + \frac{\bar{B}}{\varepsilon \bar{h}_1} \right), \quad (8)$$

and

$$\eta'(t) = \varepsilon h_1'(t) + B'(t) = \varepsilon h_1'(t) \left( 1 + \frac{B'(t)}{\varepsilon h_1'(t)} \right), \quad (9)$$

where

$$h_1'(t) = h_1(t) - \bar{h}_1. \quad (10)$$

Equations (8) and (9) show the baroclinic and barotropic contributions to the mean sea height and the sea height anomaly, respectively. Combining (9) and (10), the thickness of the upper layer is then given by

$$h_1(t) = \bar{h}_1 + \frac{1}{\varepsilon} [\eta'(t) - B'(t)]. \quad (11)$$

The geostrophic velocity in the column can be calculated for each layer from

$$\mathbf{V}_1 = f^{-1} \mathbf{k} \times \{g' \nabla h_1(x, t) + g \nabla B(x, t)\} \quad (12)$$

$$\mathbf{V}_2 = \rho_2^{-1} f^{-1} \mathbf{k} \times g \nabla B(x, t), \quad (13)$$

where  $f$  is the Coriolis parameter and  $\mathbf{k}$  is the unit vector in the  $z$  direction.

Given this background, we now need to sort these quantities out of the available data sets; i.e., upper layer thickness from the IESs and the sea-height anomalies from the Geosat altimeter data. From these the problem becomes one of computing the unknown contribution of the barotropic fields  $\bar{B}$  and  $B'$ . We can estimate the parameter  $\varepsilon$  either from available hydrographic data for the area or from relationships between the altimeter-derived SHA,  $\eta'$ , and the upper layer thickness  $h_1$ .

## 4.2. Transport Computations

In this section we describe an analysis to estimate and monitor the barotropic and baroclinic components of the transports using expression (11) derived above for upper layer thickness.

To compute the baroclinic transport we assume that the bottom layer is at rest,  $\mathbf{V}_2 = 0$  in (13), and every change of the thickness of the upper layer corresponds to a change in sea surface height, that is,  $B'(x, t) = 0$  in (9). With these conditions, the velocity of the upper layer is

$$\mathbf{V}_1(t) = \frac{g'}{f} \nabla h_1(t). \quad (14)$$

If the distance between two sites,  $a$  and  $b$ , is  $L$ , the baroclinic transport in the upper layer,  $S_{cl}(t)$ , is

$$S_{cl}(t) = \int_{-L/2}^{L/2} |\mathbf{v}_1(t)| \bar{h}_{1,ab}(t) dx = \frac{g'}{2f} \Delta h_1^2(t), \quad (15)$$

where  $\mathbf{v}_1(t)$  is the velocity component perpendicular to the section formed by the locations  $a$  and  $b$ ,  $|\mathbf{v}_1(t)| = g'[h_{1,b}(t) - h_{1,a}(t)]/(Lf)$ ,  $\bar{h}_{1,ab}(t) = [h_{1,a}(t) + h_{1,b}(t)]/2$  is the time series of the mean thermocline depth between these sites,  $\Delta h_1^2(t) = h_{1,b}^2(t) - h_{1,a}^2(t)$ , and

$$h_{1,i}(t) = \bar{h}_{1,i} + \frac{\eta'_i(t)}{\varepsilon_i} \quad (16)$$

is the thickness of the upper layer at the site  $i$ .

We compute the square of the thickness of the upper layer using (16) for sites  $a$  and  $b$  to obtain

$$\begin{aligned} h_{1,a}^2(t) &= \bar{h}_{1,a}^2 + \frac{\eta'_a(t)}{\varepsilon_a} \left[ 2\bar{h}_{1,a} + \frac{\eta'_a(t)}{\varepsilon_a} \right], \\ h_{1,b}^2(t) &= \bar{h}_{1,b}^2 + \frac{\eta'_b(t)}{\varepsilon_b} \left[ 2\bar{h}_{1,b} + \frac{\eta'_b(t)}{\varepsilon_b} \right]. \end{aligned} \quad (17)$$

The baroclinic transport between sites  $a$  and  $b$ ,  $S_{cl}(t)$ , is then

$$\begin{aligned} S_{cl}(t) &= \frac{g'}{2f} \left\{ (\bar{h}_{1,b}^2 - \bar{h}_{1,a}^2) + \frac{\eta'_b(t)}{\varepsilon_b} \left[ 2\bar{h}_{1,b} + \frac{\eta'_b(t)}{\varepsilon_b} \right] \right. \\ &\quad \left. - \frac{\eta'_a(t)}{\varepsilon_a} \left[ 2\bar{h}_{1,a} + \frac{\eta'_a(t)}{\varepsilon_a} \right] \right\}. \end{aligned} \quad (18)$$

The first term inside the curly brackets is a function of the mean upper-layer thickness at each site and gives the mean component of the baroclinic transport. The second and third terms are also functions of the sea height variability and reduced gravity in the region and provide an estimate of the eddy component of the baroclinic transport, which is

$$S'_{cl}(t) = \frac{g'}{2f} [\eta'_b(t) - \eta'_a(t)] \left\{ 2\bar{h}_1 + \frac{1}{\bar{\varepsilon}} [\eta'_b(t) + \eta'_a(t)] \right\}, \quad (19)$$

where  $\bar{\varepsilon} \approx \varepsilon_a \approx \varepsilon_b$ , and  $\bar{h}_1 \approx \bar{h}_{1,a} \approx \bar{h}_{1,b}$ .

This expression coincides with the one obtained by *Tai* [1990] for areas where  $\eta'_b + \eta'_a$  cancels. The accuracy of (18) and (19) to reproduce the values obtained using the exact expression for the two-layer model (15) depends on how well the parameters  $\varepsilon_a$  and  $\varepsilon_b$  correlate the upper layer thickness with the SHA and on the actual barotropicity of the area, as in the baroclinic transport the term  $B'$  is set equal to zero. In the following section we present a method to estimate the value of  $\varepsilon$  using IES and altimeter data simultaneously.

We now compute the mean and eddy component of the barotropic transport, using an approach similar to the baroclinic case, but considering that both layers are moving. If we assume the velocity to be independent of depth, the transport is then

$$S_{tr}(t) = \frac{\bar{D}g}{f} \Delta B(t), \quad (20)$$

where  $\bar{D}$  is the mean ocean depth between sites  $a$  and  $b$ , and  $\Delta B$  is the barotropic sea height difference between the sites. This difference can be written in terms of their mean and anomaly values as

$$\Delta B(t) = [\bar{B}_b + B'_b(t)] - [\bar{B}_a + B'_a(t)]. \quad (21)$$

The barotropic transport is then

$$S_{tr}(t) = \frac{\bar{D}g}{f} \Delta \bar{B} + \frac{\bar{D}g}{f} \Delta B'(t) = \bar{S}_{tr} + S'_{tr}(t), \quad (22)$$

where  $\Delta \bar{B} = \bar{B}_b - \bar{B}_a$ . The first and second terms in (22) are the mean and eddy components of the barotropic transport, respectively.

The barotropic transport in each of the layers can be computed by weighting the total barotropic transport with the layer's thickness, as follows:

$$S_{tr}(t) = \frac{\bar{h}_{1,ab}(t)}{\bar{D}} S_{tr}(t) + \frac{\bar{h}_{2,ab}(t)}{\bar{D}} S_{tr}(t) = S_{tr}^{up}(t) + S_{tr}^{low}(t), \quad (23)$$

where the first term and second term are the barotropic transports in the upper and lower layer, respectively.

In a barotropic ocean, where  $B' = \eta'$ , the eddy component of the barotropic transport can be estimated directly from the altimeter data. On the other hand, the mean barotropic sea height gradient in (22) cannot be directly measured; neither can altimetry discern barotropic from baroclinic sea height anomalies. In the following section and in the appendix we propose two methods to estimate this quantity, the first based on the mass or transport balance within two boxes constructed by six IESs, and the second based on the conservation of potential vorticity.

We compute the ratio between the eddy components of the upper-layer transports between sites  $a$  and  $b$  using expressions (19), (22) and (23)

$$\frac{S'_{tr}^{up}(t)}{S'_{cl}(t)} = \left[ \frac{2\bar{h}_{1,ab}(t)}{2\bar{h}_1\bar{\varepsilon} + [\eta'_a(t) + \eta'_b(t)]} \right] \frac{\Delta B'(t)}{\Delta \eta'(t)}, \quad (24)$$

where  $\bar{h}_1 \approx \bar{h}_{1,a} \approx \bar{h}_{1,b}$  is the mean upper layer thickness in the region,  $\bar{h}_{1,ab}(t)$  is the instantaneous mean depth between sites  $a$  and  $b$ , and  $\Delta B'(t)$  and  $\Delta \eta'(t)$  are the barotropic and baroclinic sea height difference between the sites, respectively. When the term  $[\eta'_a(t) + \eta'_b(t)]$  in (24) cancels, and when  $\bar{h}_1 \approx \bar{h}_{1,ab}(t)$ , the ratio is

$$\frac{S'_{tr}^{up}(t)}{S'_{cl}(t)} = \frac{1}{\bar{\varepsilon}} \frac{\Delta B'(t)}{\Delta \eta'(t)}. \quad (25)$$

For an ocean with  $\bar{\varepsilon} = 0.01$ , identical values of barotropic and baroclinic sea height differences produce a barotropic transport in the upper layer 100 times larger than the baroclinic transport. This implies that under these conditions, the eddy barotropic component is about 100 times more efficient than its baroclinic counterpart in generating transport of water masses in the upper layer.

## 5. Results

### 5.1. Reduced Gravity

We express in (9) the observed sea height anomaly,  $\eta'$ , as a sum of a baroclinic ( $\varepsilon h'_1$ ) and a barotropic ( $B'$ ) component. The time series for the thickness of the upper layer,  $h_1(t)$ , is provided by the IESs, and therefore  $h'_1(t)$  can be easily computed. The slope of the curve in (9), the curve being a straight line, is  $\varepsilon$ , which in turn is also proportional to the reduced gravity value  $g'$ . However, these reduced gravity estimates are biased when  $B'$  and  $h'_1$  are correlated, a situation often found in Gulf Stream waters (*Z. Hallock, personal communication,*

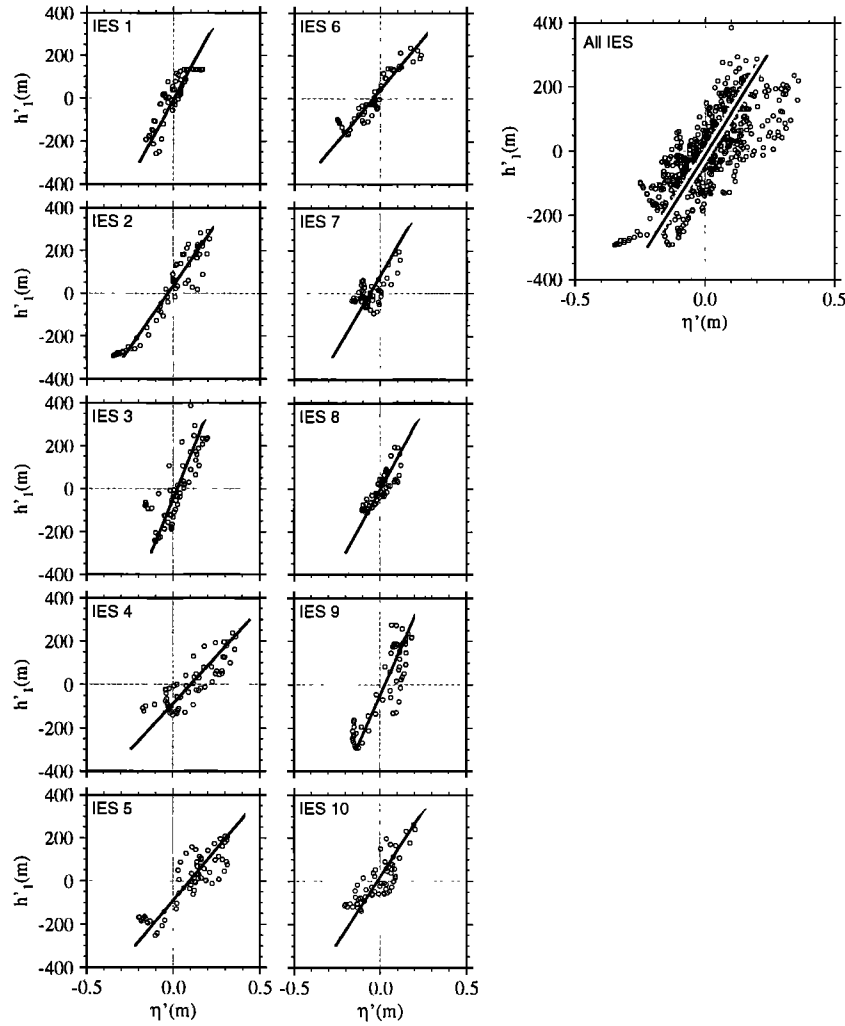


**Figure 8.** Upper layer thickness anomaly  $h'_1$  against sea height anomaly  $\eta'$  for each of the 10 sites (small panels) and for the 10 sites together (large panel). The scatter of the points in these plots is related to the mean barotropicity in the region,  $\hat{B}'$ . The measure of the stratification in the two-layer system,  $\varepsilon$ , is the slope of the straight line superimposed on top of the data. We show the values of  $\hat{B}'$  and  $\varepsilon$  at each IES location in Table 3.

1996). We quantify the temporal mean barotropic contribution at each location,  $\hat{B}'$ , from the estimate of  $B'(t)$  in the linear regression of  $\eta'$  against  $h'_1$  in (9).

Figure 8 shows the plots for  $h'_1$  as a function of  $\eta'$ , with their regression lines for each of the 10 sites (small panels) and for all the sites together (large panel). We show in Table 3 the corresponding values of  $\varepsilon$ ,  $g'$ , and the temporal mean barotropic contribution of  $B'$ ,  $\hat{B}'$ . The IES sites with higher FD and low rms sea height variability values (sites 1, 8, and 9) are associated with lower values of  $\varepsilon$ , and consequently lower values of  $g'$ , or density contrast between the two layers. We also include in Table 3 the values of the mean baroclinic component of the sea height; this is  $\varepsilon \bar{h}_1$  in (8). The lowest values of this parameter correspond to the IES sites 1, 2, 3, 8, and 9, which are locations with high FD values. In general, the mean baroclinic sea level increases in the east direction toward the center of the subtropical gyre, from 0.10 m (site 1) to 0.50 m (site 4). This result is consistent with the fact that the BC is highly baroclinic and has a higher sea level than the rest of the region. The reduced gravity values  $g'$  range approximately from 0.006 to 0.011  $\text{m s}^{-2}$  (Table 2), satisfying the relationship

that the values are higher at lower latitudes. Typical values previously obtained from regressions of dynamic height and isotherm depths from *Levitus* [1982] data are 0.013  $\text{m s}^{-2}$ .

As we mention in section 3.3, we notice that changes in  $\eta'$  due to frontal movements are approximately twice as large as those due to the passage of an eddy. However, changes in  $h'_1$  due to the passage of a front are from 2 to 4 times larger than those due to the passage of an eddy. According to (9), the values of  $B'$  should then be smaller for processes associated with the passage of the BC front than for an eddy. This implies that the eddies and rings in the Brazil-Malvinas Confluence maintain robust barotropic components as suggested in isolated eddy simulations by *Chassignet et al.* [1990].

## 5.2. Thickness of the Upper Layer and Transport Estimation From Geosat Altimeter Data

In section 4.2 we present the expressions for the time series of the baroclinic (equation (18)) and barotropic (equation (22)) transports, by combining IES and altimeter data. We now apply these results to explore the use of Geosat altimeter data

**Table 3.** Values of  $\varepsilon$ ,  $g'$ , and  $\hat{B}'$  for Each for the 10 IES Sites and for the 10 Sites Together as Obtained From a Linear Regression Between  $h'_{1,i}$  and  $\eta'$  (9)

IES site, $i$	$\varepsilon_i$	$g'_i, \text{ m s}^{-2}$	$\hat{B}'$	$\varepsilon_i \bar{h}_{1,i}, \text{ m}$
1	0.0007	0.0069	-0.0048	0.09
2	0.0009	0.0088	0.0317	0.29
3	0.0005	0.0049	-0.0219	0.26
4	0.0011	0.0108	-0.1006	0.50
5	0.0011	0.0108	-0.0951	0.49
6	0.0010	0.0098	0.0418	0.55
7	0.0007	0.0069	0.0614	0.47
8	0.0007	0.0069	0.0009	0.32
9	0.0006	0.0059	-0.0276	0.18
10	0.0008	0.0078	0.0164	0.49
All	0.0008	0.0078	0.0090	0.35

Parameters are defined in text. The last column shows the mean baroclinic sea height estimates,  $\varepsilon_i \bar{h}_{1,i}$ .

alone to provide a longer time series of upper layer thickness and transports.

The thick line in Figure 9a shows the time series for the upper layer thickness variation between sites 1 and 3, as provided directly by the IES data. The thin line shows the time series of the same parameter but with the upper layer thickness variation computed using (16) for the entire Geosat ERM period. For these computations we use the mean upper layer thickness values obtained from the IES data (Table 2), and estimate  $\varepsilon_1$  and  $\varepsilon_3$  from (9) (Table 3), as we explain in section 5.1. The estimates of the upper layer thickness variations using (16) reproduce the upper layer thickness variations measured by the IESs fairly well, with correlation coefficients better than 0.70. The remaining issue now is to assess the ability of (18) to detect the major changes in baroclinic transport values, using the upper layer thicknesses variations computed with (16).

Once we compute the upper layer thickness change between a pair of sites using the values provided either by the IESs or

by (16), we can estimate the baroclinic transport. The thick line in Figure 9b shows the time series of the baroclinic transport between sites 1 and 3, computed using (15) with the actual upper layer thicknesses provided by the IESs. The thin line shows the baroclinic transport between the same sites estimated using (18) and the upper layer thickness estimations (equation (16)).

We now present the results for the estimates of the mean baroclinic transport between selected IES sites for the Geosat ERM time period. We construct two boxes, a lower box constructed with the site pairs 1 and 3, 3 and 10, 9 and 10, and 9 and 1, and an upper box with the sites 9 and 10, 10 and 7, 8 and 7, and 7 and 9 (Figure 10). For every pair of sites in these two boxes we compute the mean baroclinic transport using (18). The thick arrows in Figure 10 show the mean baroclinic transports, which range from 7 Sv to 12 Sv toward the south and from 2 to 6 Sv toward the east. These transports are around half of those obtained by *Garzoli* [1993], who reported values of 24 Sv toward the south at 35.2° and 36.5°S and 20 Sv in the same direction between 37.7° and 38°S. *Garzoli* [1993] computes these values under the assumption that the velocity decreases linearly with depth to 1000 m, and uses dynamic heights referenced to 1000 m. On the other hand, the upper layer in our work never exceeds 700 m and includes a barotropic component with a deep pressure gradient.

To compute the barotropic transports in the upper layer,  $S_{tr}^{up}$ , we first estimate the mean barotropic sea height change, which is the term  $\Delta \bar{B}$  in (22). The mean barotropic sea height difference and flow between two sites can be estimated by applying conservation of mass or conservation of potential vorticity. Both methods provide good estimates of the mean barotropic sea height variations. However, in this section we use the conservation of mass to simultaneously estimate the mean barotropic sea height change and the mean barotropic transport in the area. We present in the appendix a method to estimate the mean barotropic sea height variation by using the conservation of potential vorticity method.

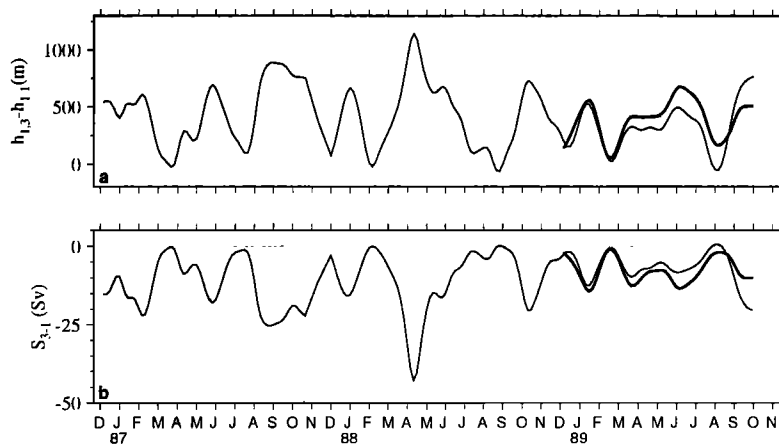


**Figure 9.** (a) Time series for the upper-layer thickness change between sites 3 and 1. The thick line corresponds to the upper layer thickness obtained from the IESs estimates during the IES study period. The thin line corresponds to the upper layer thickness change computed using (17) during Geosat ERM time period. (b) Time series for the baroclinic transport between sites 3 and 1. The thick line corresponds to the transport values computed using (15) with the values of the upper layer thickness obtained from the IESs. The thin line corresponds to the transport values computed using (18) for the Geosat ERM time period. For these estimations we obtain the mean upper layer thicknesses from the IESs time series (Table 2), while we compute the values of  $\varepsilon_1$  and  $\varepsilon_3$  using (9) (Table 3).

To compute the mass balance in the upper and lower boxes, we first calculate the total barotropic eddy transport,  $S'_{tr}$ , directly from the SHA data. We then estimate the mean barotropic sea height difference between the sides of the boxes. We compute the different mean barotropic transports between the pair of sites that form the boxes, by varying the mean barotropic sea height differences from  $-0.20$  m to  $0.20$  m, with intervals of  $0.01$  m. For every pair of sites in each box we first compute the total (mean + eddy) barotropic transports, and then calculate the upper layer barotropic transport balance within each box for every value of mean barotropic sea height change. We finally select the barotropic mean sea height differences that make the barotropic transport balance within each box approximately equal to zero. For this particular problem we find five possible solutions that make the upper layer barotropic transport balance close to zero. These solutions provide a range of barotropic mean sea height differences ranging from  $0$  to  $0.15$  m, with higher values in the center of the subtropical gyre, which is consistent with our previous results on barotropicity and baroclinicity. Figure 11 shows the average value of the five solutions for each pair of IES sites. The thin arrows in Figure 10 show the mean upper layer barotropic transports, computed from the average of the five mean upper layer barotropic transports obtained from the five solutions of the mean barotropic sea height difference. The standard deviations for these computations range from  $0.5$  Sv (between sites 1 and 9; and 9 and 8) to  $2$  Sv (between sites 7 and 8). The region between  $36^{\circ}30'S$  and  $38^{\circ}S$  appears to correspond to the confluence of northward mean barotropic flow of  $2$  Sv and

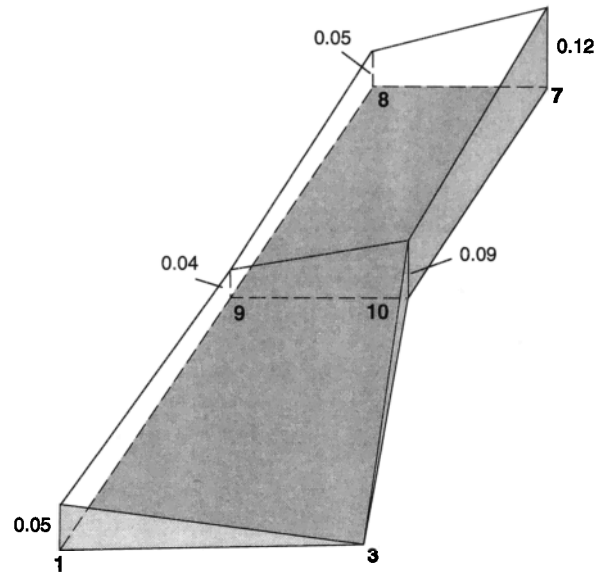


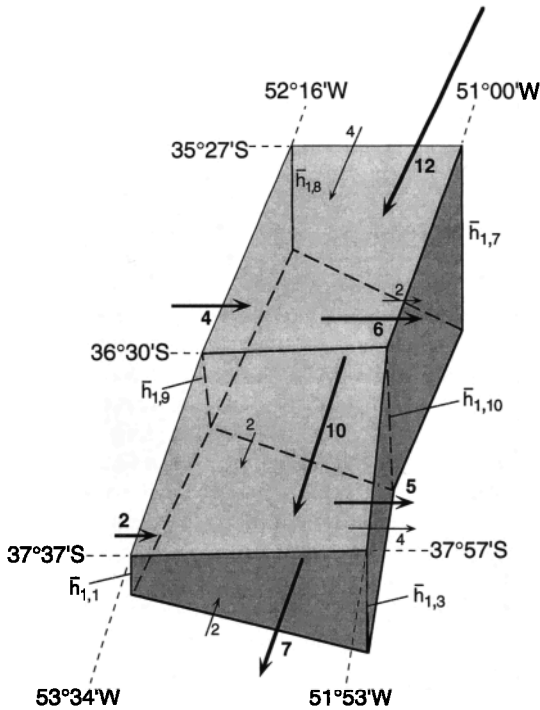
**Figure 11.** Mean barotropic sea height variations, in meters, computed for each pair of sites of the upper and lower boxes using a conservation of mass method. The bold numbers indicate the IES site, and the reference level is set at site 3.

southward mean barotropic flow of  $2$  Sv. Our results show that the upper layer barotropic transport is negligible in the east-west direction along  $53^{\circ}W$  and that it is between  $2$  and  $4$  Sv along  $51^{\circ}W$ .

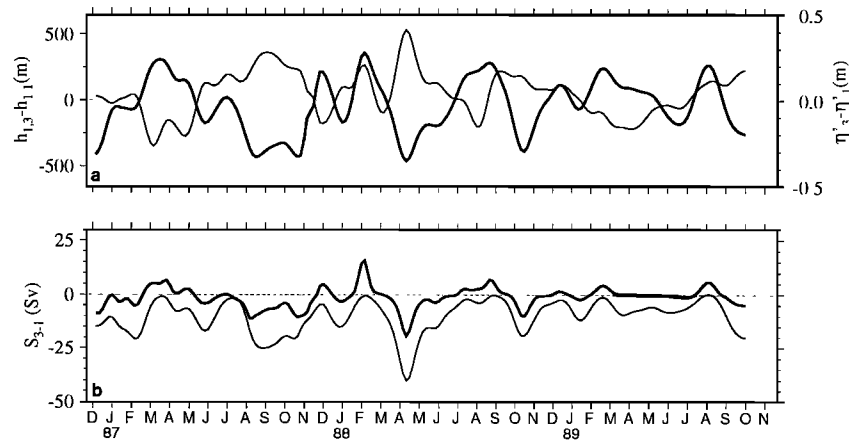
We now compute the time series of the variations of SHA and upper layer thickness, and upper layer transports between sites 1 and 3. The thick line in Figure 12a shows the time series for the SHA difference between sites 1 and 3 as obtained from the Geosat ERM data. The thin line in the same figure corresponds to the time series of the upper layer thickness difference between these same sites computed using (16). We observe the association between changes of the upper layer thickness and SHA differences between sites 1 and 3, in which an increment in the SHA difference usually corresponds to an increment in the upper layer thickness variation.

Figure 12b shows the baroclinic (thin line) and upper layer barotropic (thick line) transports between sites 1 and 3 for the same period of time, computed using (18) and the first term of (23), respectively. Positive (negative) values indicate a transport to the north (south). We use a mean barotropic sea height difference of  $0.05$  m, which produces a mean upper layer barotropic transport of around  $1$  Sv to the south. The maximum values of baroclinic and barotropic transports have periods ranging from  $2$  to  $6$  months. For short periods of time (March 1987, February 1988, August–September 1988, December 1988, and July–August 1989) the SHA and upper layer rate of change have the same sign. These episodes occur when the total barotropic transport in the upper layer is to the north.

Peterson and Stramma [1991] present a list of several estimates of transports of the BC from in situ measurements for different reference depths. Our mean upper layer transport estimates lie within the values published in the literature. However, we find a peak value of baroclinic transport of almost  $40$  Sv in April 1988 between IES sites 1 and 3 (Figure 12b) which is considerably larger than the published maximum BC transport values reported for a different period of time in the same region [Garzoli and Bianchi, 1987; Garzoli and Garrafo, 1989].



**Figure 10.** Schematic diagram of the baroclinic and barotropic transports in the upper layer for two boxes constructed from sites 7, 8, 9 and 10 (upper box) and sites 1, 3, 10 and 9 (lower box). The thick arrows indicate the mean baroclinic transport, in sverdrups, across each pair of sites during the study period. The thin arrows show the mean barotropic transport, in sverdrups, in the upper layer. The values for the upper layer thickness at each site  $i$ ,  $h_{1,i}$ , are included in Table 2.



**Figure 12.** (a) Time series for the sea height anomaly difference (thick line) and upper layer thickness difference between sites 1 and 3. (b) Time series for the baroclinic (thin line) and upper layer barotropic (thick line) transports between sites 1 and 3. Positive (negative) values indicate a transport to the north (south). The peak value of 40 Sv in the baroclinic transport is associated with the southernmost frontal location, around 48°S, found from 1987 until 1989.

From the AVHRR composites we find that the surface thermal front during that month reaches a latitude of 48°S, farther south than any other surface thermal front detected between 1984 and 1989 (Figure 3). We believe that the availability of a method to monitor the transports in the confluence region supplements previous studies on the BC frontal oscillations in the area, which are already linked to the wind forcing [Garzoli and Simionato, 1990; Smith *et al.*, 1994].

## 6. Summary and Conclusions

We combine data collected from 10 IESs and from the Geosat altimeter to investigate the dynamics of the upper layer in an area of the SW Atlantic Ocean off the Argentine coast. We also use AVHRR-derived SST composites for the area to identify surface frontal movements and mesoscale features. From IES data we find that the largest upper layer thicknesses, of around 700 m, are found at site 3 for the months of January and March and at site 7 for the month of June, which correspond to locations crossed by the jet of the Brazil Current. The mean upper layer thickness is largest, over 600 m, at the IES sites located closer to the jet of the Brazil Current. The frequency histograms of the upper layer thickness display Gaussian and non-Gaussian distributions due to the presence of the Brazil Current, the Malvinas Current, and warm and cold eddies. From altimeter data we find that the largest sea height variations, of around 0.50 m, are caused by the passage of the Brazil Current front.

We use a two-layer model to describe the dynamics of the region and to decompose the sea height and transport into their baroclinic and barotropic components. We also use the upper layer thickness anomaly and SHA data to estimate the reduced gravity values at each IES site. We estimate the mean reduced gravity value for the region is about  $0.0078 \text{ m s}^{-2}$ . We propose a method to monitor the thickness of the upper layer and the baroclinic and barotropic transports using altimetry data. We compute the time series for the upper layer thickness difference and transport between the IES sites 1 and 3 during the Geosat ERM time period. Our results indicate that the estimates of the thickness of the upper layer fit fairly well the IES-based observations, with a correlation coefficient of 0.70.

Our computations also show that the mean baroclinic transport of the Brazil Current decreases going south, from 12 Sv at 35°30'S to 10 Sv at 36°30'S to 7 Sv at 37°47'S. Figure 10 suggests that there is a recirculation of the mean baroclinic transport of around 5 Sv between 36°30'S and 37°47'S.

We propose two methods to estimate the mean barotropic sea height change, one using the balance of mass and another using the conservation of potential vorticity. The first method shows that the mean barotropic sea height change in the region ranges from 0.04 to 0.12 m. However, the conservation of potential vorticity method, presented in the appendix, gives a larger value, of around 0.90 m, which is actually a mean value of the barotropic sea height change in the region and does not refer to any specific direction. Our estimates of the upper layer mean barotropic transport indicate that this transport decreases from 4 Sv to 2 Sv between 35°30'S and 36°30'S. We also obtain a mean upper layer barotropic transport of 2 Sv to the north at 37°47'S.

The global coverage provided by Geosat and other altimeters, with the assistance of additional remote sensors such as IESs, offers useful tools to study the dynamics of the upper layer in regions of the ocean with marked contrast in stratification. Our study complements previous works on this subject [Kelly, 1991; Qiu, 1992] that use synthetic along-track mean sea heights to compute the transport from altimeter data. Our analysis is especially helpful in the Brazil-Malvinas Confluence area, where it is extremely difficult to derive synthetic profiles given the complexity of the dynamics in the region. Finally, the availability of a method to monitor the transport of the BC can supplement studies of the frontal oscillations, which have previously been linked to wind forcing.

## Appendix: Conservation of Potential Vorticity

The potential vorticity, in the absence of wind stress or other frictional effects, is a conserved quantity [Pond and Pickard, 1983]. Therefore its material or total derivative equals zero in any chosen Eulerian “control volume,” making the conservation of potential vorticity a useful tool for describing the dynamics of a current in a particular region. In a shallow water system, we define the potential vorticity  $\Pi$  as

$$\Pi = \frac{f + \zeta}{D}, \quad (\text{A1})$$

where  $f$  is the planetary vorticity or Coriolis parameter,  $\zeta$  is the relative vorticity, and  $D$  is the depth of the water column.

If we express the velocities of the upper and lower layers in terms of  $f$  and isotherm depth, the conservation of potential vorticity is [Pedlosky, 1987; Olson, 1991]

$$\Pi = \frac{f}{D} (1 + \alpha), \quad (\text{A2})$$

where  $\alpha = \zeta/f$ . In an open ocean the planetary vorticity is much larger than relative vorticity, so  $\alpha$  (in fact, the Rossby number)  $\ll 1$ . We can then re-express the conservation of vorticity by defining

$$\Pi_0 \equiv f/D, \quad (\text{A3})$$

with material derivative:

$$d\Pi_0/dt = O(\alpha). \quad (\text{A4})$$

Using the material derivative operator relative to velocity,  $d/dt = \partial/\partial t + \mathbf{V} \cdot \nabla$ , and disregarding  $O(\alpha)$ , (A3) becomes

$$\frac{d\Pi_0}{dt} = \frac{\partial\Pi_0}{\partial t} + \mathbf{V} \cdot \nabla\Pi_0, \quad (\text{A5})$$

with the velocity  $\mathbf{V}$  being the contributions from the upper and lower layers:

$$\mathbf{V} = \mathbf{V}_1 + \mathbf{V}_2. \quad (\text{A6})$$

For the simplest case in which  $\mathbf{V}_2 = 0$ , so that  $\mathbf{V} = \mathbf{V}_1$ ; we expand (A4), and with  $\partial f/\partial t = 0$  and  $\partial f/\partial x = 0$  we have

$$\frac{d\Pi_0}{dt} = -\frac{f}{h_1^2} \frac{\partial h_1}{\partial t} + \frac{g'}{fD} \frac{\partial h_1}{\partial x} \beta, \quad (\text{A7})$$

or

$$\frac{d\Pi_0}{dt} = -\frac{2\Omega \sin \phi}{h_1^2} \frac{\partial h_1}{\partial t} + \frac{g'}{R_e h_1 \tan \phi} \frac{\partial h_1}{\partial x}, \quad (\text{A8})$$

where  $\beta = \partial f/\partial y = 1/R_e \partial f/\partial \phi$ , is the variation of the Coriolis parameter with latitude,  $R_e$  is the radius of the Earth,  $\Omega$  is the angular velocity of rotation of the Earth, and  $x$  and  $y$  are the horizontal coordinates for a Cartesian system. Therefore for the case of a lower layer with zero velocity, i.e.,  $\mathbf{V}_2 = 0$ , the potential vorticity is a function of latitude, isotherm depth and time.

When  $\mathbf{V}_2 \neq 0$ , the velocity in the lower layer contributes to the total velocity, and (A4) becomes (disregarding the  $O(\alpha)$  term)

$$\frac{d\Pi_0}{dt} = \frac{\partial\Pi_0}{\partial t} + \frac{g'}{fh_1} \frac{\partial h_1}{\partial x} \beta + v_2 \frac{\partial\Pi_0}{\partial y} + u_2 \frac{\partial\Pi_0}{\partial x}, \quad (\text{A9})$$

or

$$\begin{aligned} \frac{d\Pi_0}{dt} = & \frac{f}{h_1^2} \frac{\partial h_1}{\partial t} + \frac{g'}{fh_1} \frac{\partial h_1}{\partial x} \beta + v_2 \left( \frac{\beta}{h_1} - \frac{f}{h_1^2} \frac{\partial h_1}{\partial y} \right) \\ & - u_2 \left( \frac{f}{h_1^2} \frac{\partial h_1}{\partial x} \right), \end{aligned} \quad (\text{A10})$$

where  $v_2$  and  $u_2$  are the north-south and east-west components of  $\mathbf{V}_2$ , respectively. Combining with (13) yields

$$\begin{aligned} \frac{d\Pi_0}{dt} = & \frac{f}{h_1^2} \frac{\partial h_1}{\partial t} + \frac{g'}{fh_1} \frac{\partial h_1}{\partial x} \beta + \frac{g'}{fh_1} \frac{\partial B}{\partial x} \beta - \frac{g'}{h_1^2} \frac{\partial B}{\partial x} \frac{\partial h_1}{\partial y} \\ & - \frac{g'}{h_1^2} \frac{\partial B}{\partial y} \frac{\partial h_1}{\partial x}, \end{aligned} \quad (\text{A11})$$

where  $B(x)$  is the barotropic sea height component. Alternatively, if we define

$$G(x, y, t) \equiv -\frac{f}{h_1^2} \frac{\partial h_1}{\partial t} + \frac{g'}{fh_1} \frac{\partial h_1}{\partial x} \beta, \quad (\text{A12})$$

then (13), (A3), and (A9) lead to a partial differential equation of the form

$$\frac{\partial B}{\partial y} \frac{\partial\Pi_0}{\partial x} - \frac{\partial B}{\partial x} \frac{\partial\Pi_0}{\partial y} = \frac{f}{g'} G(x, y, t), \quad (\text{A13})$$

which is readily solvable given a continuous and differentiable  $\Pi_0$  field, allowing us to estimate a mean value for  $B$ , which is  $\bar{B}$  in (8).

We make use of (A13) to estimate the barotropic sea height change  $B'$ . We use a two-dimensional spline program to resolve the data onto a 20-by-20 grid for time intervals of 5 days, to match the times in the  $\eta'$  and  $h_1'$  time series. We use a value of  $0.0078 \text{ m s}^{-2}$  for the reduced gravity, obtained from  $\varepsilon$  as derived in section 5.1. We use the assumption that for a given IES site,  $\bar{B} = 0$ , to give  $B = B'$ , as well as their gradients. We compute  $\bar{\eta}$  from (8) under the equivalent barotropic assumption, i.e., that  $B = \bar{B} = 0$ . We calculate the spatial gradients using a two-dimensional spline algorithm. The barotropic surface height  $B$  can then be readily computed using the values of  $\eta$  and  $h_1$ .

We compute the velocity of the upper and lower layers,  $\bar{V}_1$  and  $\bar{V}_2$ , using (13) and we find them to be of the order of  $0.10 \text{ m s}^{-1}$ . For this region, Gordon [1989] reports a maximum poleward geostrophic velocity of  $0.61 \text{ m s}^{-1}$  relative to 1000 dbar. A steady state condition becomes apparent when  $G(x, y, t)$  is smoothed to a 30-day interval. We find the function  $G(x, y, t)$  to be of the order of  $10^{-14} \text{ m}^{-1} \text{ s}^{-1}$  at the IES measurement sites. The derivatives of  $B$ ,  $\partial B/\partial x$ , and  $\partial B/\partial y$  are of the order of  $10^{-7} \text{ m m}^{-1}$ , and the derivatives of  $\Pi_0$  are on the order of  $10^{-13} \text{ m}^{-1} \text{ s}^{-1}$ . Thus we find that after we subtract the Jacobian of  $\Pi_0$  and  $B$  from  $G(x, y, t)$  in (A13), the result is negligibly smaller than  $G(x, y, t)$ .

Because  $G(x, y, t)$  achieves a nearly steady, but nonzero, state on a 30-day timescale, it is probable that the equivalent barotropic assumption is inappropriate for this model; there should be a nonzero mean barotropic component that varies as a function of latitude and longitude. In particular, that the area of least steadiness occurred at sites 1, 2, and 9, the southwestern corner of the array, is not surprising because this region, greatly influenced by the MC front, is subject to greater mixing and other frictional effects than other regions in the array.

From (A13) an estimate of the mean barotropic component of the sea height,  $B$ , to order of magnitude is

$$B \sim \frac{f}{g'} G \left( \frac{L}{\Pi_0} \right) L. \quad (\text{A14})$$

We use the aforementioned values and  $f \sim 7.10^{-5} \text{ rad s}^{-1}$ ,  $\Pi_0 \sim 10^{-6} \text{ m}^{-1} \text{ s}^{-1}$ , and  $L = 10^5 \text{ m}$  to obtain  $B \sim 0.89 \text{ m}$ .

This analysis allows us to estimate the barotropic sea height change in the area covered by the IESSs. However, the value of  $0.89 \text{ m}$  is only a rough estimate for the entire area and does not

refer to any specific direction. For practical purposes we assume that the mean barotropic sea height change is in the E-W direction, with higher values of  $B$  in the west. We can use this value of  $B$  in (22) to compute the mean barotropic transport between IES sites. We present this method as an alternate to the conservation of mass method used in section 5.2, due to the simplicity in estimating  $B$ .

**Acknowledgments.** The AVHRR data were collected at Estación H RTP en Alta Resolución (Buenos Aires, Argentina) by Servicio Meteorológico Nacional, Fuerza Aérea Argentina, as part of a cooperative study with the University of Miami. We thank Arthur Mariano, who kindly provided the computer code to compute the OA fields. We are particularly grateful to the reviewers of the manuscript for their valuable comments and suggestions. We also thank Victor Zlotnicki, O. Brown, and Linda Smith for helpful discussions, and Guillermo Podesta for providing the AVHRR composites, the computer code to compute the frontal densities, and comments on the manuscript. The authors also wish to thank Miriam Colwell for proofreading the manuscript, and Jean Carpenter and Rosanne Kolaczynski for helping in the preparation of some of the figures and tables. This research was supported by ONR grants N00014-89-J1144 and N00014-89-1-0166, and by grant OCE 91002541 (S.G.).

## References

- Campos, E. J. D., and D. B. Olson, Stationary Rossby waves in western boundary current extensions, *J. Phys. Oceanogr.*, **21**, 1202–1224, 1991.
- Chassignet, E. P., D. B. Olson, and D. B. Boudra, Motion and evolution of oceanic rings in a numerical model and in observations, *J. Geophys. Res.*, **95**, 22,121–22,140, 1990.
- Chelton, D. B., M. G. Schlax, D. L. Witter, and J. G. Richman, Geosat altimeter observations of the surface circulation of the Southern Ocean, *J. Geophys. Res.*, **95**, 17,877–17,903, 1990.
- Cheney, R. E., J. G. Marsh, and B. D. Beckley, Global mesoscale variability from collinear tracks of Seasat altimeter data, *J. Geophys. Res.*, **88**, 4343–4354, 1983.
- Cheney, R. E., B. C. Douglas, R. W. Agreen, L. Miller, D. L. Porter, and N. S. Doyle, Geosat altimeter geophysical data record user handbook, *NOAA Tech. Memo. NOS NGS-46*, 32 pp., Natl. Ocean Serv., Rockville, Md., 1987.
- Confluence Principal Investigators, Confluence 1988–1990, An intensive study of the southwestern Atlantic, *Eos Trans. AGU*, **71**, 1131–1133, 1137, 1990.
- Ezer, T., G. L. Mellor, D.-S. Ko, and Z. Sirkes, A comparison of Gulf Stream sea surface height fields derived from Geosat altimeter data and those derived from sea surface temperature data, *J. Atmos. Oceanic Technol.*, **10**, 76–87, 1993.
- Forbes, M. C., K. Leaman, D. Olson, and O. Brown, Eddy and wave dynamics in the South Atlantic as diagnosed from Geosat altimeter data, *J. Geophys. Res.*, **98**, 12,297–12,314, 1993.
- Garraffo, Z., S. L. Garzoli, W. Haxby, and D. Olson, Analysis of a general circulation model, 2, Distribution of kinetic energy in the South Atlantic and Kuroshio/Oyashio systems, *J. Geophys. Res.*, **97**, 20,139–20,153, 1992.
- Garzoli, S., Geostrophic velocity and transport variability in the Brazil-Malvinas Confluence, *Deep Sea Res.*, **40**, 1379–1394, 1993.
- Garzoli, S., and A. Bianchi, Time-space variability of the local dynamics of the Malvinas-Brazil Confluence as revealed by inverted echo sounders, *J. Geophys. Res.*, **92**, 1914–1922, 1987.
- Garzoli, S., and Z. Garraffo, Transports, Frontal motions and eddies at the Brazil-Malvinas Currents confluence, *Deep Sea Res.*, **36**, 681–703, 1989.
- Garzoli, S., and C. Simionato, Baroclinic instabilities and forced oscillations in the Brazil/Malvinas Confluence front, *Deep Sea Res.*, **37**, 1053–1074, 1990.
- Garzoli, S., Z. Garraffo, G. Podesta, and O. Brown, Analysis of a general circulation model product, 1, Frontal systems in the Brazil/Malvinas and Kuroshio/Oyashio regions, *J. Geophys. Res.*, **97**, 20,117–20,138, 1992.
- Gordon, A. L., Brazil-Malvinas Confluence—1984, *Deep Sea Res.*, **36**, 359–384, 1989.
- Gordon, A. L., and C. L. Greengrove, Geostrophic circulation of the Brazil-Falkland Confluence, *Deep Sea Res.*, **33**, 573–585, 1986.
- Haines, B. J., G. H. Born, G. W. Rosborough, J. G. Marsh, and R. G. Williamson, Precise orbit computation for the Geosat Exact Repeat Mission, *J. Geophys. Res.*, **95**, 2871–2885, 1990.
- Hallock, Z. R., and W. J. Teague, Sea surface height fluctuations observed simultaneously with inverted echo sounders and Geosat, *J. Geophys. Res.*, **98**, 16,341–16,349, 1993.
- Kelly, K. A., The meandering Gulf Stream as seen by the Geosat altimeter: Surface transport, position, and velocity variance from 73° to 46°W, *J. Geophys. Res.*, **96**, 16,721–16,738, 1991.
- Kelly, K. A., and S. T. Gille, Gulf Stream surface transport and statistics at 69°W from the Geosat altimeter, *J. Geophys. Res.*, **95**, 3149–3161, 1990.
- Kelly, K. A., T. M. Joyce, D. M. Schubert, and M. J. Caruso, The mean sea surface height and geoid along the Geosat subtrack from Bermuda to Cape Cod, *J. Geophys. Res.*, **96**, 12,699–12,709, 1991.
- Kim, K., and T. Rossby, On the eddy statistics in a ring-rich area: A hypothesis of bimodal structure, *J. Mar. Res.*, **37**, 201–213, 1979.
- Legeckis, R., and A. L. Gordon, Satellite observations of the Brazil and Falkland Currents—1975 to 1976 and 1978, *Deep Sea Res.*, **29**, 375–401, 1982.
- Levitus, S., Climatological atlas of the world ocean, *NOAA Prof. Pap.* **13**, 173 pp., U.S. Dep. of Commer., Silver Spring, Md., 1982.
- Mariano, A. J., and O. B. Brown, Efficient objective analysis of dynamically heterogeneous and nonstationary fields via the parameter matrix, *Deep Sea Res.*, **39**, 1255–1271, 1992.
- Matano, R., On the separation of the Brazil Current from the coast, *J. Phys. Oceanogr.*, **23**, 79–90, 1993.
- Olson, D. B., Ocean circulation, in *Encyclopedia of Earth System Science*, vol. 3, pp. 367–381, Academic, San Diego, Calif., 1991.
- Olson, D. B., R. W. Schmitt, M. Kennelly, and T. M. Joyce, A two-layer diagnostic model of the long-term physical evolution of warm-core ring 82B, *J. Geophys. Res.*, **90**, 8813–8822, 1985.
- Olson, D. B., G. P. Podesta, R. H. Evans, and O. B. Brown, Temporal variations in the separation of Brazil and Malvinas Currents, *Deep Sea Res.*, **35**, 1971–1990, 1988.
- Pedlosky, J., *Geophysical Fluid Dynamics*, 710 pp., Springer-Verlag, New York, 1987.
- Peterson, R. G., and L. Stramma, Upper-level circulation in the South Atlantic Ocean, *Prog. Oceanogr.*, **26**, 1–73, 1991.
- Podesta, G. P., O. B. Brown, and R. H. Evans, The annual cycle of satellite-derived sea surface temperature in the southwestern Atlantic Ocean, *J. Clim.*, **4**, 457–467, 1991.
- Pond, S., and G. L. Pickard, *Introductory Dynamical Oceanography*, 329 pp., Pergamon, Tarrytown, N. Y., 1983.
- Provost, C., and P.-Y. Le Traon, Spatial and temporal scales in altimetric variability in the Brazil-Malvinas Current confluence region: Dominance of the semiannual period and large spatial scales, *J. Geophys. Res.*, **98**, 18,037–18,051, 1993.
- Provost, C., V. Garçon, and S. Garzoli, Sea level variability in the Brazil and Malvinas Confluence region, *Adv. Space Res.*, **9**, 387–392, 1989.
- Qiu, B., Recirculation and seasonal change of the Kuroshio from altimetry observations, *J. Geophys. Res.*, **97**, 17,801–17,811, 1992.
- Roden, G. I., Thermohaline fronts and baroclinic flow in the Argentina Basin during the austral spring of 1984, *J. Geophys. Res.*, **91**, 5075–5093, 1986.
- Semtner, A. J., Jr., and R. M. Chervin, Ocean general circulation from a global eddy-resolving model, *J. Geophys. Res.*, **97**, 5493–5550, 1992.
- Schuessel, P., H.-Y. Shin, W. J. Emery, and H. Grassl, Comparison of satellite-derived sea surface temperatures with in-situ measurements, *J. Geophys. Res.*, **92**, 2859–2874, 1987.
- Smith, L. T., E. P. Chassignet, and D. B. Olson, Wind-forced variations in the Brazil-Malvinas Confluence region as simulated in a coarse resolution numerical model of the South Atlantic, *J. Geophys. Res.*, **99**, 5095–5117, 1994.
- Szcechowski, C., Comparison of satellite-derived Gulf Stream Front and eddy analyses with Geosat underflight data, *Mar Technol. Soc. J.*, **26**(2), 53–62, 1992.
- Tai, C.-K., Estimating the surface transport of meandering oceanic jet stream from satellite altimetry: Surface estimates for the Gulf Stream and Kuroshio extension, *J. Phys. Oceanogr.*, **20**, 860–879, 1990.
- Teague, W. J., Z. R. Hallock, G. A. Jacobs, and J. L. Mitchell, Kuroshio sea surface height fluctuations observed simultaneously with

inverted echo sounders and TOPEX/POSEIDON, *J. Geophys. Res.*, **100**, 24,987–24,994, 1995.

Watts, D. R., and T. Rossby, Measuring dynamic heights with inverted echo sounders: Results from MODE, *J. Phys. Oceanogr.*, **7**, 345–358, 1977.

Zemba, J. C., The transport and structure of the Brazil Current between 27° and 36°South, Ph.D. dissertation, Mass. Inst. of Technol., Cambridge, 1991.

---

S. Garzoli, Lamont-Doherty Earth Observatory of Columbia University, Palisades, NY 10964-8000.

G. Goni, S. Kamholz, and D. Olson, Division of Meteorology and Physical Oceanography, Rosenstiel School of Marine and Atmospheric Science, 4600 Rickenbacker Causeway, Miami, FL 33149. (e-mail: gustavo@pomelo.rsmas.miami.edu)

(Received July 31, 1995; revised March 25, 1996; accepted April 11, 1996.)